

Competing Active and Passive Interactions Drive Amoeba-like Living Crystallites and Ordered Bands

Abraham Mauleon-Amieva,^{1,2,3,4} Majid Mosayebi,^{5,6} James E. Hallett,^{1,2,3} Francesco Turci,¹ Tanniemola B. Liverpool,^{5,6} Jeroen S. van Duijneveldt,² and C. Patrick Royall^{1,2,3}

¹*H.H. Wills Physics Laboratory, Tyndall Avenue, Bristol, BS8 1TL, UK*

²*School of Chemistry, University of Bristol, Cantock's Close, Bristol, BS8 1TS, UK*

³*Centre for Nanoscience and Quantum Information, Tyndall Avenue, Bristol, BS8 1FD, UK*

⁴*Bristol Centre for Functional Nanomaterials, Tyndall Avenue, Bristol, BS8 1FD, UK*

⁵*School of Mathematics, University of Bristol, Bristol, BS8 1TW, UK*

⁶*BrisSynBio, Life Sciences Building, Tyndall Avenue, Bristol, BS8 1TQ, UK*

Swimmers and self-propelled particles are physical models for the collective behaviour and motility of a wide variety of living systems, such as bacteria colonies, bird flocks and fish schools. Such artificial active materials are amenable to physical models which reveal the microscopic mechanisms underlying the collective behaviour. Here we study colloids in a DC electric field. Our quasi-two-dimensional system of electrically-driven particles exhibits a rich and exotic phase behaviour. At low field strengths, electrohydrodynamic flows lead to self-organisation into crystallites with hexagonal order. Upon self-propulsion of the particles due to Quincke rotation, we find an ordered phase of active matter in which the motile crystallites constantly change shape and collide with one another. At higher field strengths, this “dissolves” to an active gas. We parameterise a particulate simulation model which reproduces the experimentally observed phases and, at higher field strengths predicts an activity-driven demixing to band-like structures.

Introduction

From living organisms to synthetic colloidal particles, active systems display exotic phenomena not attainable by matter at thermal equilibrium [1–4], such as swarming [5, 6], cluster-formation [7, 8] or phase separation in the absence of attractions [9–11], banding [12], and unusual crystallisation behaviour [13]. This is due to continuous energy consumption which occurs in a wide range of systems at very different lengthscales, from the cell cytoskeleton [14, 15], tissues [16] and bacterial colonies [17–20] to larger scales such as insect swarms [21], fish schools [22] and bird flocks [23]. Artificial active materials, composed of microswimmers, active colloids or vibrating granular particles [4, 7, 13, 18, 24], or even synthetically modified living systems such as bacteria [11], provide a suitable testing ground where the behaviour of active matter may be carefully probed to extract the new physical principles of this emergent class of matter.

While simple models of active particles capture some of the complex behaviour observed experimentally, for example collective motion [25–29], the link between experiment and theory in active matter is often rather qualitative. As a result, a comprehensive understanding of how and which microscopic mechanisms lead to the emergence of complex structures in experimental active systems remains elusive. Here we implement a theoretical description which is able to predict the behaviour observed in experiments. In particular, we parameterise our experimental system at the microscopic level of the interacting particles. We combine this model with particle-resolved studies of so-called Quincke rollers, active colloids which exhibit swarming and flocking [30, 31].

At low-to-moderate motility, we reveal the importance

of competing passive interactions (long-ranged attractions) driving crystallisation and activity which leads to melting-like and evaporation-like behaviour. At high motility, the role of passive and active interactions is *reversed*: activity drives demixing resulting in a banding phase, whose ordered local structures result from the repulsive core of the particles. This importance of competition between passive and active interactions is reminiscent of well-known systems such as amphiphiles, block copolymers and mixtures of charged colloids and non-absorbing polymer where competing interactions lead to modulated phases such as lamellae [32, 33], whose structures indeed resemble some we find here. Our approach shows how one may build bottom-up designs of particulate active matter with precisely controllable macroscopic behaviour.

In the Quincke rollers we study, the application of a uniform DC electric field above a critical field strength E_Q induces the directed motion of spherical colloids by coupling their translation and diffusion near a surface [30, 34]. In the absence of a field, the particles behave as conventional passive Brownian colloids. At low field strengths, while remaining non-motile, particles agglomerate into crystals due to long-ranged attractive interactions which arise from electro-osmotic flows (Fig. **A**) [35–37]. Above the critical field strength E_Q , the particles undergo Quincke rotation [38–40] and become motile (Fig. **B**) so that the electro-osmotically generated crystallites transition into a highly mobile active state reminiscent of amoebae (see Supplementary Movies 1-3, available online in <https://abrhmma0.wixsite.com/website>). Unlike “living crystals” [8], they are motile and characterised by a highly dynamic outer surface. These crys-

tallites then dissolve into an isotropic active gas as we increase the field strength. Finally at very high field strengths our simulations predict that the system undergoes banding which involves local ordering. We investigate the rich structural and dynamical properties of our system using a range of static and dynamic order parameters and in particular consider the coalescence and division of our amoeba-like motile crystals.

Results Experiments

A more complete description of the experimental setup shown schematically in Fig. A. is included in the Methods section. Briefly, we use a suspension of colloidal particles of diameter $\sigma = 2.92 \mu\text{m}$ in a non-aqueous ionic solution. Sedimentation results in a quasi 2D system with area fraction $\phi_{\text{exp}} \approx 0.05$. The sample cell is made from two indium-tin-oxide (ITO) coated glass slides separated with UV-cured resin containing spacer beads to allow the application of the electric field. The samples are imaged with bright-field optical microscopy for particle tracking. A uniform field E_0 is applied perpendicular to the two slides as represented in Fig. A, in order to enable self-propulsion due to Quincke rotation. We then translate the resultant field-dependent activity to dimensionless Péclet numbers and characterise the static and dynamic behaviour of the system. Throughout, we use the Brownian time for a colloid to diffuse its own radius in 2D, $\tau = \sigma^2/D_t \approx 9\text{s}$, as the unit of time, where D_t is the translational diffusion constant.

Simulations

The Quincke rollers are subject to forces and torques due to excluded volume repulsions, as well as self-propulsion, alignment and attractions generated by the electro-hydrodynamic interactions of the particles with their environment and each other [30, 41]. They can be modelled as *active Brownian particles* with an additional *active aligning torque*, whose active/passive forces and torques can be quantitatively specified. We implement Brownian dynamics simulations, with the following equations of motion for positions and orientations \mathbf{r}_i, θ_i .

$$\dot{\mathbf{r}}_i = \frac{D_t}{k_B T} [\mathbf{F}_i + f^p \hat{\mathbf{P}}_i] + \sqrt{2D_t} \boldsymbol{\xi}_i^t, \quad (1)$$

$$\dot{\theta}_i = \frac{D_r}{k_B T} \mathcal{T}_i + \sqrt{2D_r} \xi_i^r, \quad (2)$$

where \mathbf{F}_i is the interparticle force on the i th roller, f^p is the magnitude of the active force, $\hat{\mathbf{P}}_i = (\cos \theta_i, \sin \theta_i)$ is the direction of motion of the i th roller, \mathcal{T}_i is the torque on the i th roller which incorporates alignment terms, and $\xi_i^{t,r}$ is a Gaussian white noise of zero mean and unit variance. D_r is the rotational diffusion constant. The direct interactions \mathbf{F}_i include a ‘‘hard’’ core and long-range attraction, the latter to model the electrohydrodynamic contribution. Further details of the model and the sim-

ulation parameters, and the procedure by which the parameters were mapped to the experiment may be found in the Methods and Supplementary Materials (SM).

Determining the Péclet number

Before moving to the discussion of our results, we first describe our mapping of field strength to Péclet number between experiment and simulation. We obtain the bare translational diffusion coefficient of the passive system D_t measured at equilibrium. Particle velocity v , and the characteristic time scale for the rotational diffusion $\tau_r = D_r^{-1}$ for a dilute sample with area fraction $\phi \approx 0.001$ are obtained from the fitting to the mean square displacement (MSD) of active particles in the dilute (gas) regime,

$$\langle \Delta r^2(t) \rangle = 4D_t t + \frac{v^2 \tau_r^2}{3} \left[\frac{2t}{\tau_r} + \exp\left(\frac{-2t}{\tau_r}\right) - 1 \right]. \quad (3)$$

To extract the parameters of Eq. 3 from the experiments we consider a series of similarly dilute samples. We estimate the dimensionless Péclet number as $Pe = 3v\tau_r/\sigma$, for each measured velocity in the different states obtained in the experiment. The Péclet number is significantly enhanced by Quincke rotation. However, since this is related to the threshold field strength E_Q where Quincke rotation is initiated, we find that for low field strengths, Pe is small and only weakly dependent on the field, $E_0 \ll E_Q$, $Pe \sim 0$. Once the particles become motile, for our system the two appear to be roughly linearly coupled ($E_0 > E_Q$, $Pe \sim E_0$, see SM Fig. S1).

We now present our main findings. First we consider the phase behaviour of the system as a function of the activity, represented by the Péclet number which we obtain from measuring particle mobility. At zero field strength ($Pe = 0$), we obtain Brownian hard discs which form a dilute fluid with area fraction $\phi \approx 0.05$. Upon increasing the field strength, the system exhibits a novel phase behaviour owing to a coupling between non-equilibrium electrohydrodynamic interactions due to solvent flow and electrically induced activity (Quincke rotation).

Crystallisation

Particle condensation to form crystallites emerges at low field strength, e.g. $Pe \approx 1 \times 10^{-4}$ ($E_0 = 9.9E_Q$). This is due to the long-ranged electrohydrodynamic interactions (Fig. A) [41]. In our experiments, colloids act as dielectric regions perturbing the electric charge distribution, therefore inducing a flow of ions with a component tangential to the substrate [41]. In the vicinity of such an electro-osmotic flow, the particles experience transverse motion leading to the formation of crystallites (Fig. A).

Activity-induced phase transitions

Upon increasing the field strength, we can exploit the Quincke mechanism that triggers spontaneous rotation (Fig. B) to study the behaviour of self-propelled rollers. For this to occur, the viscous torque acting on the particle

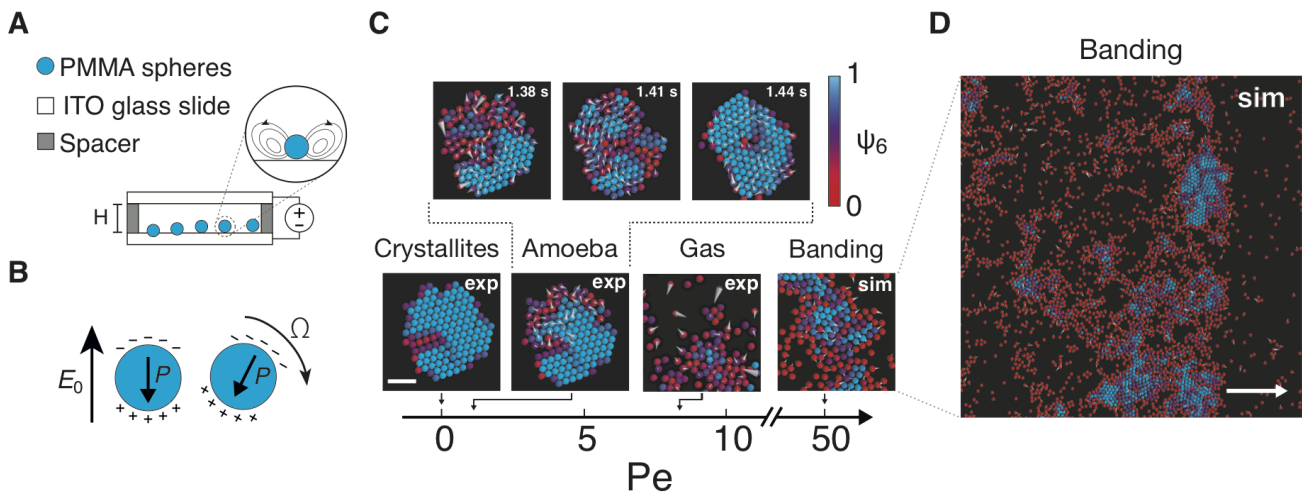


FIG. 1. **Phase diagram of Quincke Rollers as a function of activity.** **A Experimental set-up.** Colloidal particles are suspended and confined within a sample cell made of conductive glass slides. The induced electrohydrodynamic flow is represented with dashed lines in the amplified illustration. This flow field leads to long-ranged electrohydrodynamic interactions between the particles [41]. **B. Schematic representation of mechanism of Quincke rolling.** The charge distribution around the sphere forms a dipole oriented inversely to the field direction, and any fluctuation in the dipole orientation leads to particle rotation with a constant angular speed Ω . The field-dependent activity is translated to the Péclet number, as described in the text. **C. Phase behaviour as a function of Péclet number.** In the low activity regime, electrohydrodynamic interactions due to flow fields (see inset in Fig. A) result in (passive) crystallite formation. On increasing the activity, e.g. $Pe = 1.5$ ($E_0 = 19.4E_Q$, with $E_Q \approx 6.2 \times 10^4 \text{ V} \cdot \text{m}^{-1}$), the particles self-propel sufficiently that the dynamics change markedly (see upper sequence), and the active crystals split and coalesce with one another. With a further increase of activity, the crystallites melt and we find an active gas. In the regime accessible to our simulations, we find banding at a somewhat higher area fraction of $\phi = 0.08$. Scale bar is $10 \mu\text{m}$. Colorbar indicates the local hexagonal order of coloured particles, ψ_6 . **D. Banding.** Zoomed out rendering of the band formation in simulations. White arrow indicates the direction of propagation.

must be overcome, hence the field needs to be sufficient to initiate rolling ($> E_Q$). When increasing the activity above $Pe = 1.5$ ($E_0 = 19.4E_Q$), we observe crystallite motility, coalescence and splitting, yet the local hexagonal symmetry remains, as can be seen in certain bacteria colonies [20] and chiral swimmers [42]. We term this an “amoeba phase”, since the motility leads the aggregate to constantly reshape in a fashion reminiscent of the motion of amoebae, as shown by the time sequence in Fig. c (also see Supplementary Movies 1-3).

On further increasing the field to $E_0 = 29.8E_Q$ ($Pe = 7.8$), Quincke rotation triggers breakdown of the active crystallites into an “active gas” of colloidal rollers undergoing displacement in random directions, Fig. C. Previously, it was shown experimentally that the increase in area fraction results in homogeneous polar phases and vortices [30, 31]. At higher field strength, our simulations predict that around $Pe \gtrsim 35$, the system exhibits a non-equilibrium phase transition to a banded state. These bands form perpendicular to the direction of particle motion (which self-organizes into a strongly preferred direction). (see Supplementary Movies 4 and 5). This is reminiscent of banding observed in earlier experiments [30], but here the area fraction is very much higher, leading to local hexagonal order. In our simulations, we see one

band in the box. We leave the analysis of whether this is activity-driven micro-phase separation, or full demixing for a later finite-size scaling analysis. This local hexagonal order within the bands contrasts with the unstructured bands seen in the Vicsek model [12].

Analysis of the Local Structure

Having qualitatively introduced the behaviour we encounter in our system in Fig. , we now proceed to consider the phase transitions in more detail. In order to determine the nature of the transitions we require suitable order parameters. We first consider the structural properties of the phases we encounter — passive fluid, passive crystal, active crystallite (“amoebae”), active gas and bands. Given the richness of the phase behaviour, it is unlikely that one single order parameter will prove sufficient, and we find this to be the case. We begin with the 2D bond-orientational order parameter, $\psi_6 = (1/N) \sum_{i=1}^N |\psi_6^i|$. Perfect hexagonal ordering is indicated by $\psi_6 = 1$, whereas a completely disordered configuration gives $\psi_6 = 0$. See Methods for more details of ψ_6 .

In Fig. 2A, we plot the average ψ_6 as a function of Pe for both experiment and simulation, under our mapping of Pe between the two and in the inset we show the data with respect to the applied electric field. In the SM, we

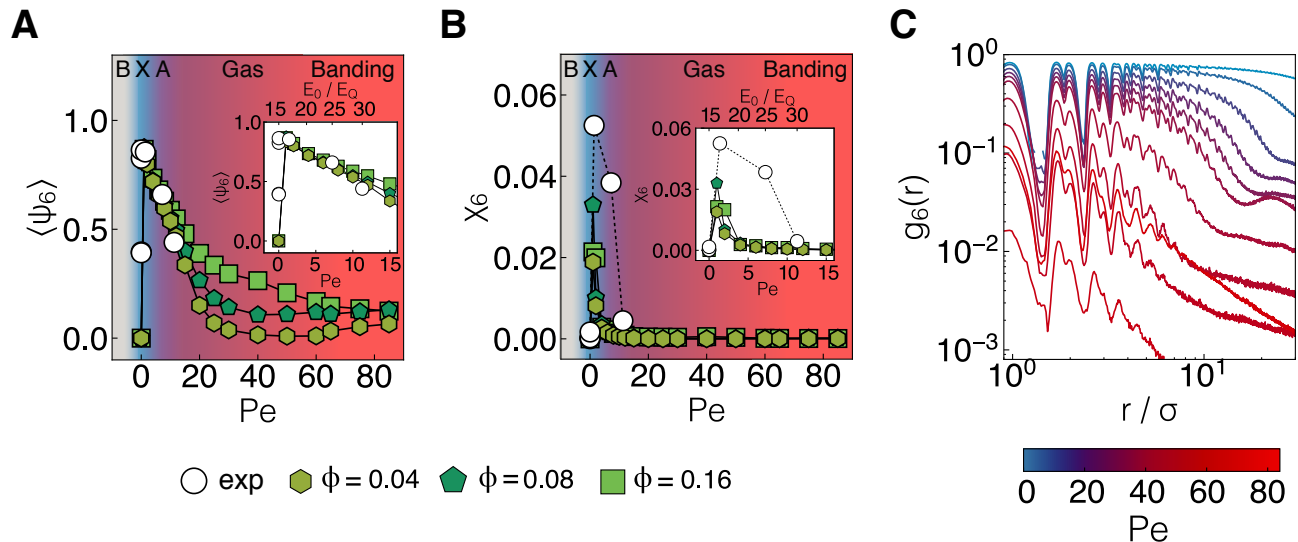


FIG. 2. **Changes in local structure as a function of field strength for Quincke rollers.** **A.** Local order determined with the bond-orientational parameter ψ_6 upon increasing field strength. **B.** Fluctuations of the bond-orientational parameter χ_6 upon increasing field strength as defined in the text. Dashed line indicates the onset of motility, which distinguishes crystalline and amoeba states. Insets in **A** and **B** show data plotted with respect to the applied field strength. **C.** Orientational correlation functions $g_6(r)$ for Pe as indicated in the color bar. Data obtained from simulations with $\phi = 0.08$. In **A** and **B** and in subsequent figures, the phases are denoted as B - Brownian fluid, X - crystallites, A - amoebae, (active) gas and banding. Insets in **A** and **B** are zoom in sections indicating E_0 values.

show ψ_6 with respect to the electric field strength E_0 . We emphasise that, given the simplicity of our model, and of our mapping, the agreement between experiment and simulation is remarkable in the experimentally accessible regime ($Pe \lesssim 8$). We find almost no ordering for the passive Brownian system (at $E_0 = 0$ or $Pe = 0$). With a slight increase in the field strength to $E_0 = 9.9E_Q$, we observe a rapid rise in ψ_6 to ≈ 0.9 that corresponds to the crystallisation transition driven by the electrohydrodynamic interactions. In this regime, the system is composed of many crystallites that barely move. It is possible that there may be a condensed liquid (or hexatic) phase [43], although this is not apparent in our data, and the transition appears first-order within the field strengths we have sampled. We believe this to be similar to equilibrium 2D attractive systems undergoing crystallisation and move on to consider the activity-driven transitions.

Increasing the activity further into the amoeba phase, ψ_6 starts to decrease. However, ψ_6 remains significantly above zero indicating the amoeba clusters are crystal-like. While this state is far-from-equilibrium, the ψ_6 value exhibits temporal fluctuations consistent with a steady state (Supplementary Fig. S2). We infer that to distinguish the (passive) crystallites from the amoebae, some kind of dynamic order parameter may prove suitable, and return to this below. At larger Pe ($10 \lesssim Pe \lesssim 40$), the value of ψ_6 , drops markedly, as the amoebae “dissolve” into the active gas, apparently in a continuous fashion.

Finally at very high Pe ($Pe \gtrsim 40$), upon the emergence of banding, a form of motility-driven phase separation, the value of ψ_6 again shows signs of increase for $\phi < 0.16$.

To gain further insight into these transitions, in Fig. 2B we plot the fluctuations in the hexatic bond-orientation order parameter which we take as $\chi_6 = \langle \psi_6^2 \rangle - \langle \psi_6 \rangle^2$ where the average is over different snapshots. Further details are provided in the Methods. At low Péclet numbers, we see good agreement between the experiment and simulation, but when the motility is higher, the simulations decay towards the active gas faster than the experiments. However, we find no enhancement in χ_6 around the amoeba-gas phase boundaries, indicating that the transition is a cross-over rather than a first-order-like transition between different phases.

To quantify the spatial correlations in ψ_6 , in Fig. 2C, we plot $g_6(r)$ defined as,

$$g_6(r = |\mathbf{r}_i - \mathbf{r}_j|) = \langle \psi_6^{i*} \psi_6^j \rangle \quad (4)$$

where ψ_6^i is the (complex) value of the hexatic bond-orientation order parameter for particle i at position \mathbf{r}_i . At low Pe , we observe long-ranged orientational correlations in the crystal and amoeba regimes. Such correlations are significantly shorter-ranged for the active gas. Interestingly, for the largest Pe in the banding regime, we find that the bond-orientational order parameter is correlated over a larger domain than in the gas regime.

Therefore, formation of the bands not only increases ψ_6 , but also enhances its spatial correlations.

Dynamical Analysis

In our analysis of the local structure in Fig. 2, we noted that some kind of dynamical order parameter would be appropriate to distinguish the crystallites from the amoebae. In Fig. 3, we use such an order parameter to perform this analysis, the overlap [13],

$$Q(t) = \left\langle \frac{1}{N} \sum_{i=1}^N \exp - \left(\frac{[\mathbf{r}_i(t'+t) - \mathbf{r}_i(t')]^2}{a^2} \right) \right\rangle_{t'} \quad (5)$$

which we evaluate at $a = \sigma$. We fit the resulting dynamic correlation functions with a stretched exponential form, $Q(t) = \exp[-(t/\tau_\alpha)^b]$, as shown in Fig. 3A to determine a timescale for relaxation in our system, τ_α . We plot this timescale against the Péclet number in Fig. 3B.

Most striking in the crystal-amoeba transition is the massive drop in relaxation time, Fig. 3B: at a total of *six decades*, this is a very substantial change dynamical change for particle-resolved studies of colloids, active or passive [44]. The crystallites are effectively solids, while the amoebae exhibit timescales of colloidal liquids, even though their structure is crystalline. Despite this precipitous drop in relaxation time, we find that the transition from crystallites to amoeba is apparently continuous in nature. We thus conclude that the crystallite-amoeba and amoeba-active gas transitions we have found are both continuous, at least insofar as we can detect.

Characteristics of the Active and Passive Crystallites

In Fig. 2, our ψ_6 bond-orientational order parameter gave somewhat limited insight as to the nature of the crystallite-amoeba transition, as both exhibit hexagonal local symmetry. Therefore we now seek other structural measures. In Fig. 4A, we consider the fractal nature of the crystallites formed, be they passive or active. The images in Fig. and Supplementary Movies 1-3 hint that, if the amoebae are rather mobile, then the “interface” between the “amoeba” and its surroundings may be broadened, leading to more particles at the interface and a lower fractal dimension. Specifically, for each cluster we count the number of particles identified on the boundary N_b . In the case of compact clusters, this should scale with the number of particles in the cluster as N^ν with $\nu = 1/2$. Figure 4A shows the different nature of the passive and active clusters with $\nu \approx 3/4$ and $5/6$ respectively, indicating a rougher boundary for the active clusters.

Figure 4B shows how the mean cluster size varies in different regimes. The system is composed of a few large clusters at very low Pe . Upon increasing the activity, those big clusters break up to smaller ones until in the gas regime where the system is dominated by monomers. Consistent with our previous observations, the cluster

size is non-monotonic, with an increase of the mean cluster size with the formation of the bands at large Pe . Note that in the regime where our simulations indicate banding, finite size effects in the simulations (which have $N = 10000$ particles) may influence the cluster size somewhat as the bands span the simulation box. The same holds for the passive crystals at low field strength.

Nature of the Transitions at Higher Activity: Amoeba to Active Gas and Active Gas to Ordered Bands

In addition to the transitions we have already discussed, we encounter more at higher field strength. Firstly, the amoebae “dissolve” to form an “active gas”. At the densities we consider, this transition is characterised by a substantial – but continuous – drop in the ψ_6 bond-orientational order parameter (Fig. 2A) consistent with our discussion of the continuous change in dynamics above.

At higher field strengths, we encounter banding, strong density fluctuations perpendicular to the preferred direction of travel. Interestingly, these bands exhibit some degree of local order, as the value of the bond-orientational order parameter $\langle \psi_6 \rangle \approx 0.2$. While far from indicating full hexagonal order ($\langle \psi_6 \rangle = 1$), this is nevertheless significantly larger than zero. Furthermore, as we can see in Fig. C, some particles are in a very high state of crystalline order (appearing blue), although most are not. Rather striking, in the case of the transition to the banded phase is the alignment between the dipoles of the Quincke rollers, which defines the direction of rotation (see SM for details). In Fig. 4C, we see a very strong increase in the alignment upon banding, suggesting that this is a suitable order parameter in this case.

Amoeba Coalescence and Splitting

As Supplementary Movies 1 and 3 show, the amoebae are highly dynamic. Here we analyse their coalescence and splitting. It is intriguing to compare it with coalescence and splitting (or break-off) of liquid droplets [45, 46]. However there are several key differences between the two situations. Both coalescence and break-off of liquid drops in passive systems are macroscopic driven processes that are clearly *not* in a steady state [45, 46], while here the amoeba phase is apparently a non-equilibrium steady state. Furthermore here the clusters are locally ordered. We consider the behaviour at the particle scale and emphasise the 2d nature of the system. Nevertheless one may ask if insights about the steady-state behaviour of our active system can be obtained by considering the behaviour of a driven passive system that is not in a steady state. It is noteworthy that in passive systems there is a strong asymmetry between liquid drop coalescence and break-off – break-off dynamics is very distinct from that of coalescence, reflecting the fact that end-points of the two processes are rather different. In contrast, thermodynamic equilibrium is a steady state with vanishing currents and hence one expects sym-

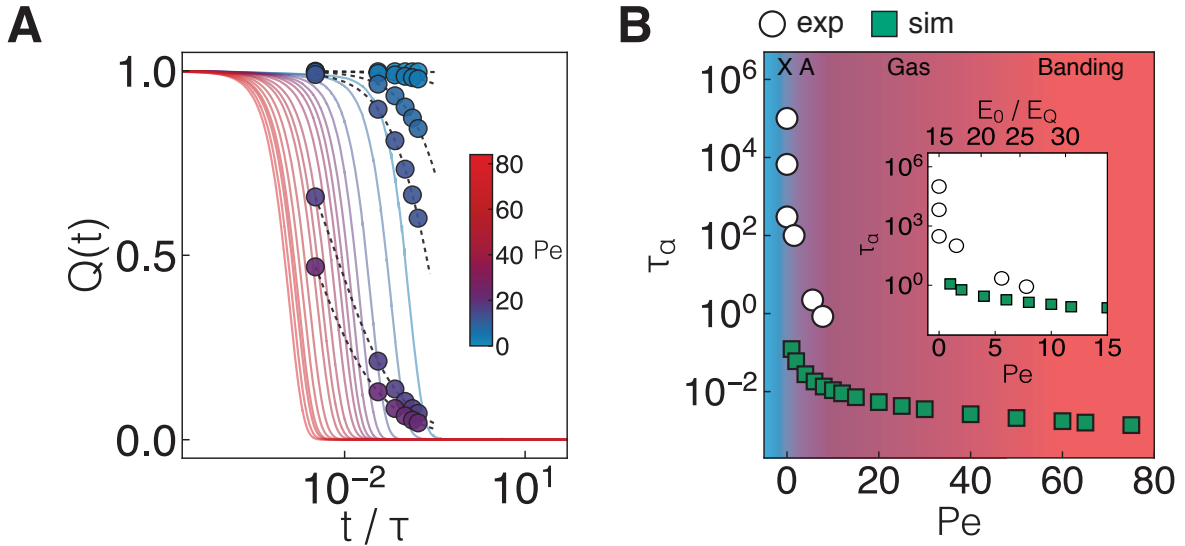


FIG. 3. **Dynamics of the Quincke Rollers across various phases.** **A.** Dynamical overlap function $Q(t)$, using Eq. 5. Coloured circles are experimental data, and solid lines are obtained from simulations. Dashed lines are stretched exponential fits as described in the text. Color bar indicates the correspondent Pe for each line. Data are scaled by the Brownian time τ . **B.** Relaxation time τ_α from stretched-exponential fitting to symbols and lines. Inset shows the relaxation time plotted as a function of the field strength in the regime accessible to the experiments.

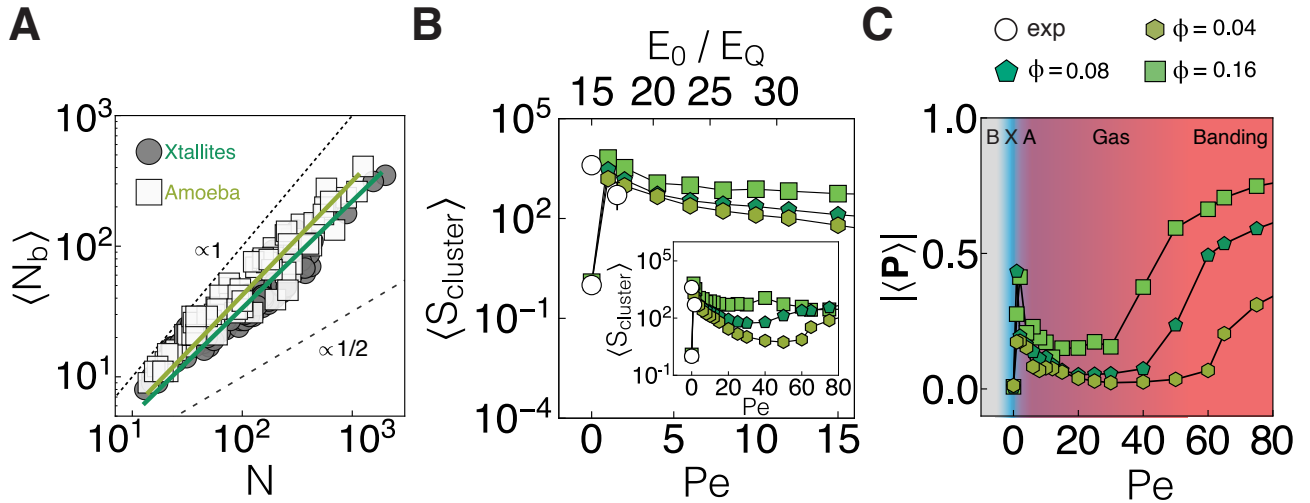


FIG. 4. **Characteristics of the clusters formed by the Quincke rollers.** **A.** Interfacial broadening in crystallites and amoebae. This is averaged over all the particles sampled in the experiment at each state point. **B.** Size of clusters as a function of activity. Inset is a zoom in to indicate the field values. **C.** Dipolar orientations as function of field strength.

metry between coalescence and break-off at equilibrium. However it is not at all obvious if there would be a symmetry between the dynamics of coalescence and break-off in the amoeba phase because it is a non-equilibrium steady-state. That is to say, while of course the micro-

scopic equations of motion in this non-equilibrium system are not expected to exhibit time-reversal symmetry, we enquire whether this is apparent at the level of the coalescence and splitting behaviour in the Amoeba phase. In particular, we consider whether we can distinguish the

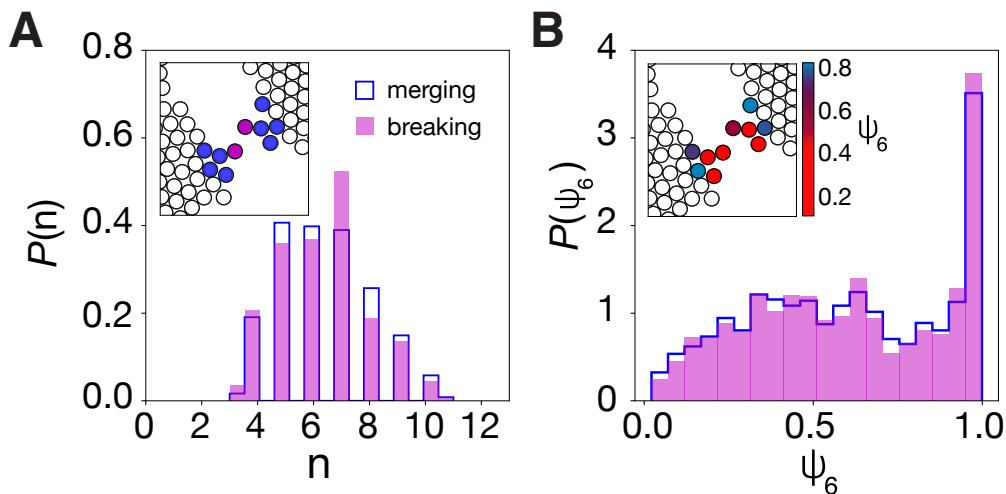


FIG. 5. “Amoeba” coalescence and splitting. **A.** Distribution of number of shell (blue) particles for all amoebae either splitting or coalescing. Inset: Snapshot prior to a coalescence event between two clusters. Purple particles represent the nearest boundary particles between clusters, and blue particles are the first shell of particles around purple particles. **B.** Distribution of the local ψ_6 for the same breaking and merging events. Inset: Same snapshot now showing the local hexagonal order for the same particles.

pathways by which coalescence and splitting occurs.

We analyse the coalescence and break-off events in the amoeba phase as follows. First distinct “amoebae” are identified (See SM). To investigate the morphological changes, we account for the change in number of particles per “amoeba” and measure the nearest distance between boundary particles in different clusters. This yields the particles which first form the link between two “amoebae” in the case of coalescence and those where the last point of contact remains in the case of splitting (Fig. 5A, inset).

Having the pair of particles involved in coalescence and splitting, we identify the number of particles within a distance of 1.1σ and analyse the local ψ_6 . In Fig. 5, we plot the resulting distributions of the number of particles n in the neighbourhood and the local ψ_6 with time running forwards and backwards. Since the distributions appear rather similar within our statistics, we infer that our analysis does not reveal any breaking of time-reversal symmetry, consistent with recent work with active Janus colloids which considered aggregation and fragmentation rates [47]. Thus this non-equilibrium steady state is fundamentally different to the highly asymmetric case of droplet coalescence and break-off in driven passive liquids [45, 46].

Discussion

In conclusion, we have shown that the Quincke roller system exhibits a rich and complex phase behaviour. We have also developed a minimal model of the experimental system which captures all the phenomena observed in experiment, and in fact predicts further phase transitions at activities beyond the experimental regime. We find transitions between passive fluid, crystal, amoeba-

like active crystallites, active gas and an ordered banding phase. We have used a variety of static and dynamic order parameters to probe the nature of these transitions, and find that they are continuous in nature except the (passive) fluid-crystal transition which is consistent with first-order. We have analysed coalescence and splitting events in the “amoeba” phase, and find that it does not show significant deviations from time-reversal symmetry.

For our simulation model, we have quantitatively parameterised the components of the Quincke roller system by treating the electrohydrodynamic attraction with a long-ranged potential, “hard” core, active force and electrohydrodynamic alignment terms. Remarkably, when we rescale our results to compare the same Péclet numbers in experiments and simulations, we obtain a quantitative agreement between the two. With our model, we have revealed that a key ingredient of the phase behaviour is the interplay between *active* and *passive* interactions. At low mobility, (electrohydrodynamic) passive attractions lead to condensation into crystals, which melt with an increase in activity. Conversely, at high activity, the situation is reversed: activity leads to banding where the (passive) repulsive core controls the local structure. Our work opens the way to using simple, intuitive minimal models which correctly capture the competition between active and passive interactions to describe, *quantitatively*, the macroscopic physical behaviour of complex active systems which are far-from-equilibrium.

Materials and Methods

Experimental setup

Our experimental model consists of poly(methyl methacrylate) (PMMA) spheres of diameter, $\sigma = 2.92\mu\text{m}$ determined with SEM. These are suspended in

a 5 mM solution of dioctyl sulfosuccinate sodium (AOT) in hexadecane. Imaging and DC field application take place in sample cells made of two indium tin oxide (ITO)-coated glass slides (Diamond Coatings, BO-X-20, 100 nm thick). A separating layer of $H = 16.2 \mu\text{m}$ between the slides is made using larger polymer beads and UV-curable adhesive (Norland 81). The uniform field is applied by connecting the slide to a power supply (Elektro Automatik, PS-2384-05B). Image sequences are obtained using brightfield microscopy (Leica DMI 3000B) with a 20x objective and a frame rate of 100 fps. Individual colloids are identified and particle co-ordinates are tracked using standard methods [48].

Determination of the critical strength

We follow the description of Lemaire and co-workers [39, 49] to estimate the critical field strength, E_Q . The spontaneous rotation of particles, known as Quincke rotation, strongly depends on the charge distribution at the particle-liquid interface and the respective charge relaxation times, given by $\tau_{p,l} = \epsilon_{p,l}/s_{p,l}$, where $\epsilon_{p,l}$ and $s_{p,l}$ are the dielectric constant and conductivity of the particle and the liquid respectively. In the case of having $\tau_l > \tau_p$, the induced dipole \mathbf{P}_{exp} is stable with respect of field direction. On the other hand with $\tau_p > \tau_l$, \mathbf{P}_{exp} is unstable with respect to the field direction (see Fig. 1A in main text), and any perturbation results in an electrostatic torque $\mathcal{T}^e = \mathbf{P}_{\text{exp}} \times \mathbf{E}$, from the dipole rotation. Nevertheless, even if $\tau_p > \tau_l$ is satisfied, \mathcal{T}^e needs to overcome the viscous torque exerted on the particle by the liquid to initiate rotation, $\mathcal{T}^H = -\alpha\omega$, where the angular velocity is given by ω and $\alpha = \pi\eta\sigma^3$ is the rotational friction coefficient. We use polymethyl methacrylate colloids of diameter $\sigma = 2.92 \mu\text{m}$, with $\epsilon_p = 2.6\epsilon_0$, and a 5 mM AOT/hexadecane solution with $\eta = 2.78 \text{ mPA}$,

$s_l \approx 10^{-8} \Omega^{-1} \text{ m}^{-1}$ [50], $s_p \approx 10^{-14} \Omega^{-1} \text{ m}^{-1}$ [39] and $\epsilon_l \approx 2\epsilon_0$ for our system. The critical threshold is given by

$$E_Q = \frac{1}{2} [\pi\epsilon_l\sigma^3(\chi^0 - \chi^\infty)\tau_{\text{MW}}\alpha^{-1}]^{1/2}, \quad (6)$$

where the polarisability factors

$$\chi^0 = \frac{s_p - s_l}{s_p + 2s_l} \quad (7)$$

and

$$\chi^\infty = \frac{\epsilon_p - \epsilon_l}{\epsilon_p + 2\epsilon_l} \quad (8)$$

account for the conductivities and permittivities of the particle and liquid respectively. The characteristic dipole relaxation timescale is given by the Maxwell-Wagner time,

$$\tau_{\text{MW}} = \frac{\epsilon_p + 2\epsilon_l}{s_p + 2s_l}. \quad (9)$$

Microscopic model of effective interactions in Quincke rollers

Following Ref. [30], we consider a pairwise alignment interaction between rollers that leads to a torque on particle i

$$\mathcal{T}_i = -\frac{\partial \mathcal{R}_{\text{align}}}{\partial \theta_i};$$

$$\mathcal{R}_{\text{align}} = - \sum_{j, |\mathbf{r}_{ij}| \leq r_{c1}} \left(A_1 \hat{\mathbf{P}}_i \cdot \hat{\mathbf{P}}_j + A_2 (\hat{\mathbf{P}}_i - \hat{\mathbf{P}}_j) \cdot \hat{\mathbf{r}}_{ij} + A_3 \hat{\mathbf{P}}_j \cdot (2\hat{\mathbf{r}}_{ij}\hat{\mathbf{r}}_{ij} - \mathbf{I}) \cdot \hat{\mathbf{P}}_i \right) \quad (10)$$

where $\hat{\mathbf{P}}_i = (\cos \theta_i, \sin \theta_i)$ is the direction of motion of the i th roller, and \mathbf{r}_{ij} is the separation between rollers i and j . This has the minimum number of terms required to describe the electro-hydrodynamically induced alignment interactions with the correct symmetry and whose range is set by the distance between plates in the experimental setup. We truncate $\mathcal{R}_{\text{align}}$ at $r_{c1} = 3.0\sigma$, where σ is the particle diameter. We note that angular momentum is not conserved by these dynamics.

The electro-osmotic long-ranged attraction [41] is modelled by a truncated and shifted (at $r_{c2} = 5.0\sigma$) potential of the form $\mathcal{H}_{\text{attr}} = -A_4 \exp(-\kappa r)/r^2$, where $\kappa = 1/3\sigma^{-1}$ is the inverse screening length. The excluded volume interactions between rollers are represented by

a repulsive Weeks-Chandler-Anderson (WCA) interaction of the form $\mathcal{H}_{\text{exc}} = 4\epsilon((\sigma/r)^{12} - (\sigma/r)^6) + \epsilon$, where $\epsilon = k_B T$ is the energy unit of the model. The WCA potential is truncated at $r_{c3} = 2^{1/6}\sigma$.

The coupling parameters in the alignment interactions are estimated to be $A_1 = 0.93k_B T$, $A_2 = 0.33k_B T$ and $A_3 = 0.48k_B T$ for our experimental conditions (see SM for more details), and we chose the attraction strength to be $A_4 = 10k_B T$. We verified that the qualitative phase behaviour of the model remains the same if we vary the strength of the long-ranged attraction. We note that we have parametrised A_1, A_3 from the single particle dynamics in the dilute gas phase, the attractive interactions A_2, A_4 are determined from the experimental parame-

ters. Further details are given in the SM.

Simulation details. —

Brownian dynamics simulations were performed on a 2D system composed of $N = 10000$ interacting Quincke rollers. We integrate the over-damped Langevin equations (Eqs. 2) using the stochastic Euler scheme with a time step of $dt = 10^{-5}\tau$. In our simulations, the interparticle force on the i th roller $\mathbf{F}_i = -\nabla_i(\mathcal{H}_{\text{attr}} + \mathcal{H}_{\text{exc}})$ while the torque on the i th roller $\mathcal{T}_i = -\partial\mathcal{R}_{\text{align}}/\partial\theta_i$. The particle diameter σ , thermal energy $\epsilon = k_B T$ and Brownian time $\tau = \sigma^2/D_t$ are chosen as basic units for length, energy and time, respectively. We take $D_r = 3D_t/\sigma^2$, as expected for a spherical particle in the low-Reynolds-number regime. We study the phase behaviour of the system as a function of two dimensionless parameters; Péclet number $Pe = f^p\sigma/k_B T$ and the area fraction $\phi = \frac{N\pi\sigma^2}{4L^2}$, where L is the linear size of the simulation box.

Order parameter details. —

Here we take the mean of the bond-orientational order parameter ψ_6 across N particles

$$\psi_6 = \frac{1}{N} \sum_{j=1}^N |\psi_6^j|. \quad (11)$$

The value of the order parameter for each particle is

$$\psi_6^j \equiv \frac{1}{Z_j} \sum_{k=1}^{Z_j} \exp(i6\theta_k^j) \quad (12)$$

where the particle i is subject to a propulsion force of magnitude f^p whose direction changes due to the alignment interaction and noise ξ_i . Note that because the simulations are strictly in 2D, the direction of the dipole \mathbf{P} in Eq. 15 is that of the rotation, *i.e.* the direction of

where Z_j is the co-ordination number of particle j obtained from a Voronoi construction and θ_k^j is the angle made between a reference axis and the bond between particle j and its k th neighbour. $\psi_6 = 1$ indicates perfect hexagonal ordering, whereas completely disordered structures give $\psi_6 = 0$. Fig. 2A shows that for a passive Brownian system there is almost no hexatic order.

We quantify the fluctuations in ψ_6 by defining the susceptibility

$$\chi_6 \equiv \langle \psi_6^2 \rangle - \langle \psi_6 \rangle^2 \quad (13)$$

where $\psi_6^2 = 1/N \sum_{j=1}^N |\psi_6^j|^2$.

Supplementary Materials Microscopic model of Alignment Interactions in Quincke Rollers

The following description is based on a microscopic model describing the dynamics of a population of colloidal rollers due to Quincke rotation. The direct interactions are detailed in the Methods, and are captured in the force \mathbf{F}_i in Eq. 14. Here we consider the alignment terms. The equations of motion for the i th self-propelled particle are given by the following Langevin equations, where for the rotational case we have rewritten the version in the main text to explicitly consider the effective alignment interaction.

$$\dot{\mathbf{r}}_i = \frac{D_t}{k_B T} [\mathbf{F}_i + f^p \hat{\mathbf{P}}_i] + \sqrt{2D_t} \boldsymbol{\xi}_i^t \quad (14)$$

and

$$\dot{\theta}_i = -\frac{D_r}{k_B T} \frac{\partial}{\partial \theta_i} \sum_{j \neq i} \mathcal{R}_{\text{align}}(\mathbf{r}_{ij}, \hat{\mathbf{P}}_i, \hat{\mathbf{P}}_j) + \sqrt{2D_r} \xi_i^r \quad (15)$$

self-propulsion, rather than the (3D) induced dipole of the experimental system \mathbf{P}_{exp} mentioned above.

Introduced by Caussin and Bartolo [30], the effective alignment interaction $\mathcal{R}_{\text{align}}$ reads

$$\mathcal{R}_{\text{align}}(\mathbf{r}, \hat{\mathbf{P}}_i, \hat{\mathbf{P}}_j) = -A_1(r) \hat{\mathbf{P}}_i \cdot \hat{\mathbf{P}}_j - A_2(r) \hat{\mathbf{r}} \cdot (\hat{\mathbf{P}}_i - \hat{\mathbf{P}}_j) - A_3(r) \hat{\mathbf{P}}_j \cdot (2\hat{\mathbf{r}}\hat{\mathbf{r}} - \mathbf{I}) \cdot \hat{\mathbf{P}}_i \quad (16)$$

having $\hat{\mathbf{r}} \equiv \mathbf{r}/r$. The coefficients $A_1(r)$, $A_2(r)$ and $A_3(r)$

incorporates the microscopic parameters and are given by:

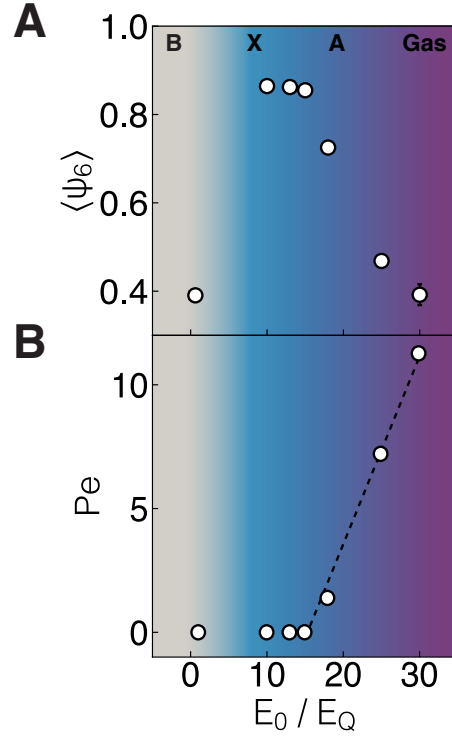


FIG. S6. **a.** Mean local hexagonal order parameter. **b.** Péclet number as a function of field strength deduced from experimental measurement at low area fraction (see main text for details). As in the main text, B denotes Brownian fluid (i.e. low field strength), X (passive) crystals, A amoeba and gas is the active gas.

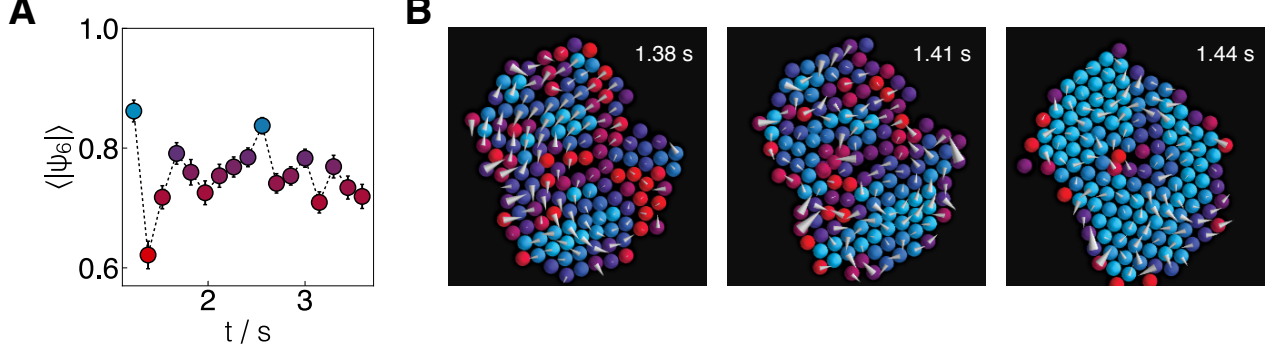


FIG. S7. **a.** Mean hexagonal order parameter in time for amoeba aggregates. **b.** Frame time sequence from Fig. 1c in the main text. Colours on particles indicate the local hexagonal order, ψ_6^i (see main text for details)

$$A_1(r) = 3\tilde{\mu}_s \frac{\sigma^3}{8r^3} \Theta(r) + 9 \left(\frac{\mu_\perp}{\mu_r} - 1 \right) \left(\chi^\infty + \frac{1}{2} \right) \left(1 - \frac{E_Q^2}{E_0^2} \right) \frac{\sigma^5}{32r^5} \Theta(r) \quad (17. 1)$$

accounting for the short-ranged hydrodynamic interactions and electrostatic couplings that promote the alignment of directions between particles i and j . Here, μ_\perp and μ_r are the mobility coefficients depending on the liquid viscosity and the distance d between the surface

and particle respectively. From the expressions in [51–54] we obtain $\chi^\infty = 0.08$, $\tilde{\mu}_s = 11$ and $\mu_\perp / \mu_r = 1.5$.

The electrostatic repulsion and the electrohydrodynamic interactions coupling are encoded in the $A_2(r)$ and $A_3(r)$ coefficients respectively,

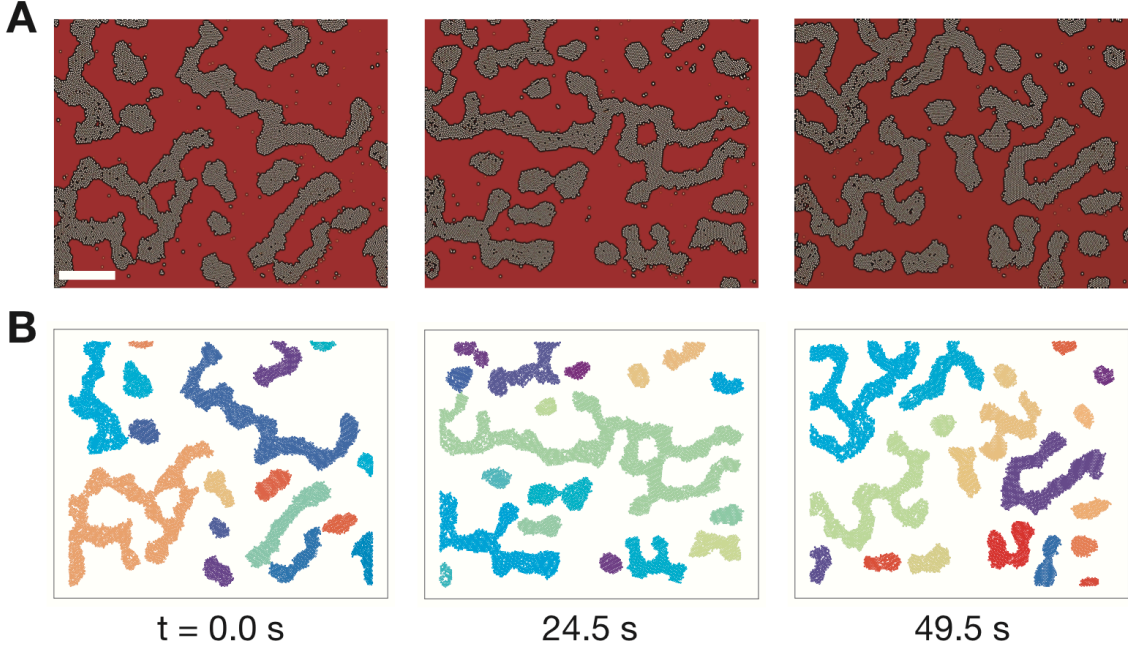


FIG. S8. **a.** Image sequence of amoeba clusters. Scale bar is $100 \mu\text{m}$. **b.** Single cluster are shown in different colours.

$$A_2(r) = 6 \left(\frac{\mu_{\perp}}{\mu_r} - 1 \right) \sqrt{\frac{E_0^2}{E_Q^2} - 1} \left[\left(\chi^{\infty} + \frac{1}{2} \right) \frac{E_0^2}{E_Q^2} - \chi^{\infty} \right] \frac{\sigma^4}{16r^4} \Theta(r) \quad (17.2)$$

$$A_3(r) = 2\tilde{\mu}_s \frac{\sigma^2}{4r^2} \frac{\sigma}{2H} + \left[\tilde{\mu}_s \frac{\sigma^3}{8r^3} + 5 \left(\frac{\mu_{\perp}}{\mu_r} - 1 \right) \left(\chi^{\infty} + \frac{1}{2} \right) \left(1 - \frac{E_Q^2}{E_0^2} \right) \frac{\sigma^5}{32r^5} \right] \Theta(r) \quad (17.3)$$

where the hydrodynamic and electrostatic couplings are screened over distances proportional to the chamber distance, $H = 16.2 \mu\text{m}$. A more detailed description can be found in Refs. [30], and [31]. We estimate such coefficients considering the experimental field intensity under which we observe the active gas phase ($1.85 \times 10^6 \text{Vm}^{-1}$), and average them over distances $r \in [\sigma, 3\sigma]$. For convenience we approximate the screening function as $\Theta(r) = 1$ if $r \leq H/\pi$ and $\Theta(r) = 0$ otherwise.

Under these assumptions, we obtain

$$A_1 = 0.93k_B T \quad (17.4)$$

$$A_2 = 0.33k_B T \quad (17.5)$$

$$A_3 = 0.48k_B T \quad (17.6)$$

Supplementary Movies

Supplementary Movie 1

Amoeba aggregates — Finite-size amoeba clusters displaying collective rotation. The interaction between amoeba aggregates leads to merging. Movie is coloured with a glow effect for clarity. Colloid diameter $\sigma = 2.92 \mu\text{m}$. Field strength, $E_0 = 19.4E_Q$, and $\text{Pe} = 1.5$. Frame acquisition at 100 fps, movie played at 34 fps [55].

Supplementary Movie 2

Amoeba phase — Movie shows the experimental trajectory of an amoeba-like aggregate. The colourbar indicates the local hexagonal order parameter ψ_6^i for each particle. Fluctuations of the order parameter result as the aggregates merge and break. White arrows indicate the instantaneous collective displacement. Colloids diameter $\sigma = 2.92 \mu\text{m}$. Field strength, $E_0 = 19.4E_Q$, and $\text{Pe} = 1.5$. Frame acquisition at 100 fps, movie played at

17 fps [55].

Supplementary Movie 3

Experimental phase transition — Transition of an isolated cluster with the increase on E_0 . The transition goes from a highly ordered and dynamically arrested state to an isotropic state of Quincke rollers. The colourbar indicates the local hexagonal order parameter ψ_6^i . Particles in blue possess high hexagonal order, whereas the order is poor in particles in red. Colloids of diameter $\sigma = 2.92 \mu\text{m}$. Field strength $E_0 \in [9.9, 29.8]E_Q$, and $\text{Pe} \in [10^{-4}, 11.3]$. Frame acquisition at 100 fps, movie played at 17 fps [55].

Supplementary Movie 4

Onset of banding — Thick bands (of tens of particles) form as particle trajectories undergo alignment. The bands propagate through an isotropic state. $\text{Pe} = 50$ [55].

Supplementary Movie 5

Onset of banding — Same data as Supplementary Movie 4, zooming out sequence. $\text{Pe} = 50$ [55].

Acknowledgements

The authors would like to thank Denis Bartolo, Olivier Dauchot, Jens Eggers, Mike Hagan, Rob Jack, Cristina Marchetti, Sriram Ramaswamy, Thomas Speck and Chantal Valeriani for helpful discussions. CPR, JH and FT would like to acknowledge the European Research Council under the FP7 / ERC Grant agreement n° 617266 “NANOPRS”. AMA is funded by CONA-CyT. TBL and MM are supported by BrisSynBio, a BBSRC/EPSRC Advanced Synthetic Biology Research Center (grant number BB/L01386X/1). Part of this work was carried out using the computational facilities of the Advanced Computing Research Centre, University of Bristol.

References and Notes

-
- [1] Marchetti, M. *et al.* Hydrodynamics of soft active matter. *Rev. Mod. Phys.* **85**, 1143 (2013).
 - [2] Schweitzer, F. *Brownian Agents and Active Particles* (Springer-Verlag, Berlin, Heidelberg, 2003).
 - [3] Ramaswamy, S. The Mechanics and Statistics of Active Matter. *Annu. Rev. Condens. Matter Phys.* **1**, 323–345 (2010). 1004.1933.
 - [4] Bechinger, C., Di Leonardo, R., Löwen, H., Reichhardt, C. & Volpe, G., G. abd Volpe. Active particles in complex and crowded environments. *Rev. Mod. Phys.* **88**, 045006 (2016).
 - [5] Ariel, G. *et al.* Swarming bacteria migrate by Lévy Walk. *Nat. Commun.* **6**, 8396 (2015).
 - [6] Narayan, V., Ramaswamy, S. & Menon, N. Long-Lived Giant Number Fluctuations in a Swarming Granular Nematic. *Science* **317**, 105–108 (2007).
 - [7] Theurkauff, I., Cottin-Bizonne, C., Palacci, J., Ybert, C. & Bocquet, L. Dynamic clustering in active colloidal suspensions with chemical signaling. *Phys. Rev. Lett.* **108**, 1–5 (2012). 1202.6264.
 - [8] Palacci, J., Sacanna, S., Steinberg, A. P., Pine, D. J. & Chaikin, P. M. Living Crystals of Light-Activated Colloidal Surfers. *Science* **339**, 936–940 (2013).
 - [9] Cates, M. E. & Tailleur, J. Motility-Induced Phase Separation. *Annual Review of Condensed Matter Physics* **6**, 219–244 (2015). 1507.05135.
 - [10] Buttinoni, I. *et al.* Dynamical Clustering and Phase Separation in Suspensions of Self-Propelled Colloidal Particles. *Phys. Rev. Lett.* **110**, 238301 (2013). 1305.4185.
 - [11] Schwarz-Linek, J. *et al.* Phase separation and rotor self-assembly in active particle suspensions. *Proc. Natl. Acad. Sci.* **109**, 4052–4057 (2012). arXiv:1404.2263v1.
 - [12] Chaté, H., Ginelli, F., Grégoire, G. & Raynaud, F. Collective motion of self-propelled particles interacting without cohesion. *Phys. Rev. E* **77**, 046113 (2008).
 - [13] Briand, G. & Dauchot, O. Crystallization of Self-Propelled Hard Discs. *Phys. Rev. Lett.* **117**, 1–5 (2016). 1605.03080.
 - [14] Jülicher, F., Kruse, K., Prost, J. & Joanny, J.-F. Active behavior of the cytoskeleton. *Phys. Rep.* **449**, 3–28 (2007).
 - [15] Sanchez, T., Chen, D. T., DeCamp, S. J., Heymann, M. & Dogic, Z. Spontaneous motion in hierarchically assembled active matter. *Nature* **491**, 431–434 (2012).
 - [16] Park, J.-A. *et al.* Unjamming and cell shape in the asthmatic airway epithelium. *Nature Mater.* **14**, 1040–1049 (2014).
 - [17] Pedley, T. & Kessler, J. Hydrodynamic phenomena in suspensions of swimming microorganisms. *Annual Review of Fluid Mechanics* **24**, 313–358 (1992).
 - [18] Zhang, H. P., Be’er, A., Florin, E.-L. & Swinney, H. L. Collective motion and density fluctuations in bacterial colonies. *Proc. Natl. Acad. Sci.* **107**, 13626–13630 (2010).
 - [19] Lushi, E., Woiland, H. & Goldstein, R. E. Fluid flows created by swimming bacteria drive self-organization in confined suspensions. *Proc. Nat. Acad. Sci.* **111**, 9733–9738 (2014).
 - [20] Petroff, A. P., Wu, X. L. & Libchaber, A. Fast-moving bacteria self-organize into active two-dimensional crystals of rotating cells. *Phys. Rev. Lett.* **114**, 1–6 (2015).
 - [21] Sinhuber, M. & Ouellette, N. T. Phase coexistence in insect swarms. *Phys. Rev. Lett.* **119**, 178003 (2017).
 - [22] Katz, Y., Tunstrom, K., Ioannou, C. C., Huepe, C. & Couzin, I. D. Inferring the structure and dynamics of interactions in schooling fish. *Proc. Natl. Acad. Sci.* **108**, 18720–18725 (2011). arXiv:1604.05974v2.
 - [23] Cavagna, A. *et al.* Scale-free correlations in starling flocks. *Proc. Natl. Acad. Sci.* **107**, 11865–11870 (2010). 0911.4393.
 - [24] Volpe, G., Buttinoni, I., Vogt, D., Kümmerer, H.-J. & Bechinger, C. Microswimmers in patterned environments. *Soft Matter* **7**, 8810 (2011). 1104.3203.
 - [25] Vicsek, T., Czirók, A., Ben-Jacob, E., Cohen, I. & Shochet, O. Novel Type of Phase Transition in a System of Self-Driven Particles. *Phys. Rev. Lett.* **75**, 1226–1229 (1995).
 - [26] Grégoire, G. & Chaté, H. Onset of Collective and Cohesive Motion. *Phys. Rev. Lett.* **92**, 025702 (2004). 0401208.
 - [27] Redner, G. S., Hagan, M. F. & Baskaran, A. Structure and dynamics of a phase-separating active colloidal fluid. *Phys. Rev. Lett.* **110**, 1–5 (2013). 1207.1737.
 - [28] Fodor, É. *et al.* How Far from Equilibrium Is Active Matter? *Phys. Rev. Lett.* **117**, 1–6 (2016). 1604.00953.

- [29] Zöttl, A. & Stark, H. Hydrodynamics Determines Collective Motion and Phase Behavior of Active Colloids in Quasi-Two-Dimensional Confinement. *Phys. Rev. Lett.* **112**, 118101 (2014). 1309.4352.
- [30] Bricard, A., Caussin, J.-B., Desreumaux, N., Dauchot, O. & Bartolo, D. Emergence of macroscopic directed motion in populations of motile colloids. *Nature* **503**, 95–98 (2013).
- [31] Bricard, A. *et al.* Emergent vortices in populations of colloidal rollers. *Nat. Commun.* **6**, 1–8 (2015).
- [32] Andelman, D. & Seul, M. Domain shapes and patterns: The phenomenology of modulated phases. *Science* **267**, 476–483 (1995).
- [33] Ciach, A. Universal sequence of ordered structures obtained from mesoscopic description of self-assembly. *Phys. Rev. E* **78**, 061505 (2008).
- [34] Jákli, A., Senyuk, B., Liao, G. & Lavrentovich, O. D. Colloidal micromotor in smectic A liquid crystal driven by DC electric field. *Soft Matter* **4**, 2471 (2008).
- [35] Yeh, S.-R., Seul, M. & Shraiman, B. I. Assembly of ordered colloidal aggregates by electric-field-induced fluid flow. *Nature* **386**, 57–59 (2000).
- [36] Ristenpart, W. D., Aksay, I. A. & Saville, D. A. Assembly of colloidal aggregates by electrohydrodynamic flow: Kinetic experiments and scaling analysis. *Phys. Rev. E - Stat. Nonlinear, Soft Matter Phys.* **69**, 1–8 (2004).
- [37] Zhang, K.-Q. & Liu, X. Y. In situ observation of colloidal monolayer nucleation driven by an alternating electric field. *Nature* **429**, 739–743 (2004).
- [38] Quincke, G. Ueber Rotationen im constanten electrischen Felde. *Ann. der Phys. und Chemie* **295**, 417–486 (1896).
- [39] Pannacci, N., Lobry, L. & Lemaire, E. How insulating particles increase the conductivity of a suspension. *Phys. Rev. Lett.* **99**, 2–5 (2007).
- [40] Das, D. & Saintillan, D. Electrohydrodynamic interaction of spherical particles under Quincke rotation. *Phys. Rev. E* **87**, 1–14 (2013).
- [41] Nadal, F. *et al.* Electrically induced flows in the vicinity of a dielectric stripe on a conducting plane. *Eur. Phys. J. E* **9**, 387–399 (2002).
- [42] Shen, Z., Würger, A. & Lintuvuori, J. S. Hydrodynamic self-assembly of active colloids: chiral spinners and dynamic crystals. *Soft Matter* (2019).
- [43] Bernard, E. P. & Krauth, W. Two-step melting in two dimensions: First-order liquid-hexatic transition. *Phys. Rev. Lett.* **107**, 155704 (2011).
- [44] Ivlev, A., Löwen, H., Morfill, G. E. & Royall, C. P. *Complex Plasmas and Colloidal Dispersions: Particle-resolved Studies of Classical Liquids and Solids* (World Scientific Publishing Co., Singapore Scientific, 2012).
- [45] Eggers, J., Lister, J. R. & A., S. H. Coalescence of liquid drops. *J. Fluid Mech.* **401**, 293–310 (1999).
- [46] Eggers, J. & Villermaux, E. Physics of liquid jets. *Rep. Prog. Phys.* **71**, 036601 (2008).
- [47] Ginot, F., Theurkauff, I., Detcheverry, F., Ybert, C. & Cottin-Bizonne, C. Aggregation-fragmentation and individual dynamics of active clusters. *Nature Commun.* **9**, 696 (2018).
- [48] Crocker, J. & Grier, D. Methods of Digital Video Microscopy for Colloidal Studies. *J. Colloid Interface Sci.* **179**, 298–310 (1996). 96.
- [49] Pannacci, N., Lemaire, E. & Lobry, L. DC conductivity of a suspension of insulating particles with internal rotation. *Eur. Phys. J. E* **28**, 411–417 (2009).
- [50] Schmidt, J. *et al.* Conductivity in nonpolar media: Experimental and numerical studies on sodium AOT-hexadecane, lecithin-hexadecane and aluminum(III)-3,5-diisopropyl salicylate-hexadecane systems. *J. Colloid. Int. Sci.* **386**, 240–251 (2012).
- [51] O’Neill, M. E. & Stewartson, K. On the slow motion of a sphere parallel to a nearby plane wall. *J. Fluid Mech.* **27**, 705 (1967).
- [52] Goldman, A., Cox, R. & Brenner, H. Slow viscous motion of a sphere parallel to a plane wall—II Motion through a quiescent fluid. *Chem. Eng. Sci.* **22**, 637–651 (1967).
- [53] Goldman, A., Cox, R. & Brenner, H. Slow viscous motion of a sphere parallel to a plane wall—I Motion through a quiescent fluid. *Chem. Eng. Sci.* **22**, 637–651 (1967).
- [54] Liu, Q. & Prosperetti, A. Wall effects on a rotating sphere. *J. Fluid Mech.* **657**, 1–21 (2010).
- [55] Supplementary movies available online in <https://abrhmma0.wixsite.com/website>.